Quantification of probabilistic ignition thresholds of polymer-bonded explosives with microstructure defects

Yaochi Wei, Seokpum Kim, Yasuyuki Horie, and Min Zhou

Citation: Journal of Applied Physics **124**, 165110 (2018); doi: 10.1063/1.5031845
View online: https://doi.org/10.1063/1.5031845
View Table of Contents: http://aip.scitation.org/toc/jap/124/16
Published by the American Institute of Physics

Quantification of probabilistic ignition thresholds of polymer-bonded explosives with microstructure defects

Yaochi Wei,[1] Seokpum Kim,[1,2] Yasuyuki Horie,[3] and Min Zhou[1,a)]
[1]*The George W. Woodruff School of Mechanical Engineering, School of Materials Science and Engineering, Georgia Institute of Technology, Atlanta, Georgia 30332-0405, USA*
[2]*Manufacturing Demonstration Facility, Oak Ridge National Laboratory, P.O. Box 2008, Oak Ridge, Tennessee 37831, USA*
[3]*Air Force Research Lab, Munitions Directorate, 2306 Perimeter Road, Eglin AFB, Florida 32542, USA*

(Received 31 March 2018; accepted 9 October 2018; published online 29 October 2018)

Microscopic defects such as voids and cracks in an energetic material significantly influence its shock sensitivity. So far, there is a lack of systematic and quantitative study of the effects of cracks both experimentally and computationally, although significant work has been done on voids. We present an approach for quantifying the effects of intragranular and interfacial cracks in polymer-bonded explosives (PBXs) via mesoscale simulations that explicitly account for such defects. Using this approach, the ignition thresholds corresponding to any given level of ignition probability and, conversely, the ignition probability corresponding to any loading condition (i.e., ignition probability maps) are predicted for PBX 9404 containing different levels of initial grain cracking or interfacial debonding. James relations are utilized to express the predicted thresholds and ignition probabilities. It is found that defects lower the ignition thresholds and cause the material to be more sensitive. This effect of defects on shock sensitivity diminishes as the shock load intensity increases. Furthermore, the sensitivity differences are rooted in energy dissipation and the consequent hotspot development. The spatial preference in hotspot distribution is studied and quantified using a parameter called the defect preference ratio (r_{pref}). Analyses reveal that defects play an important role in the development of hotspots and thus have a strong influence on the ignition thresholds. The findings are in qualitative agreement with reported trends in experiments. *Published by AIP Publishing.*
https://doi.org/10.1063/1.5031845

I. INTRODUCTION

The performance, reliability, and survivability against mechanical insults of energetic materials significantly depend on the heterogeneous microstructures of the materials.[1] As a result, defects, as an unavoidable source of microstructure heterogeneities, play a crucial role in determining the overall behavior of the materials. It is important to understand and quantify the role of defects in order to develop new materials and tailor materials for applications. Polymer-bonded explosives (PBXs) which consist of at least two constituents—energetic granules and a polymer binder—require sophisticated manufacturing processes and inevitably contain heterogeneous intragranular and interfacial defects.[2] For example, Fig. 1 is a microscopic image of a hot-pressed PBX specimen.[3] It manifests defects in the forms of intragranular cracks in the explosive granules and debonding at the grain-binder interfaces commonly seen in such materials. Analysis of the effects of the defects is important and intrinsically challenging. There have been experimental studies on the effect of the defects on shock sensitivity of PBXs. Baillou *et al.*[4] studied PBX containing cyclotrimethylene trinitramine (RDX) grains and hydroxyl-terminated polybutadiene (HTPB) binder and found that the sensitivity increases with both the number and size of grain defects. Van der Steen *et al.*[5] found that defects formed on grain surfaces during casting can make PBX more sensitive to shock loading. Borne's experiments[6,7] on RDX- and HMX-based composites substantiate these findings and further pointed out that the influence of defects on the sensitivity decreases as shock pressure increases. However, there has been little systematic study on why and how the defects are related to shock sensitivity. Furthermore, there is a lack of quantification of the effects, as defect content in PBX is difficult to measure[8] and hard to control[9] in experiments. Given a certain amount of defects in a PBX, is it possible to know how much the impact sensitivity of a PBX would change? A computational approach can avoid some of the practical challenges and provide answers to this question as it allows explicit consideration of both initial and evolving defects and pertinent mechanical and thermal processes.

In this paper, a numerical framework is used to predict the ignition threshold of PBXs with initial defects in the forms of transgranular cracks and interfacial debonding sites (interfacial cracks). The computational model explicitly captures the effects of microstructures including random constituent morphology, size distribution of energetic granules, initial configuration of defects, properties of binder, and grain-binder interfacial behavior. The framework is based on a Lagrangian cohesive finite element method (CFEM), and the recent developments[1,10–14] of the computational capability allow mechanical and thermal processes such as elasto-visco-plasticity, elasto-viscoelasticity, fracture, crack propagation, frictional heating along the cracks, and heat conduction to be

a)Author to whom correspondence should be addressed: min.zhou@gatech.edu. Tel.: 404-894-3294, Fax: 404-894-8336.

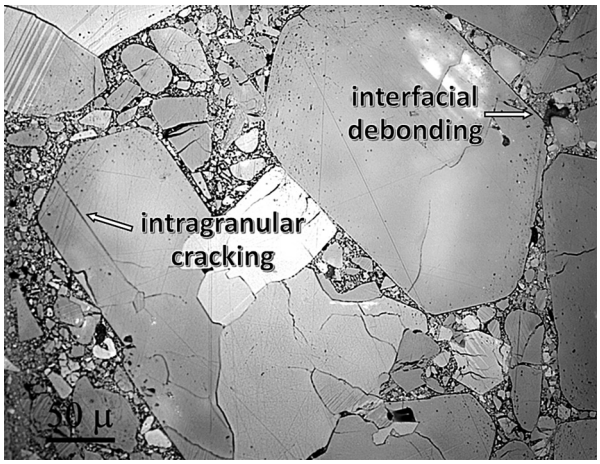

FIG. 1. Intragranular and interfacial cracks in a hot-pressed PBX specimen. Reproduced with permission from Skidmore *et al.*, in 11th Symposium (International) on Deonation, Snowmass Village, CO, 1998. Copyright Office of Naval Research, 1998.

effectively tracked. Since James and Lambourn's observation[15] substantiates the equivalence between the detonation event and the existence of critical hotspots initiating a thermal runaway, it is unnecessary in this paper to explicitly assess the issue of subsequent burn following a hotspot reaching criticality. Instead, we only focus on the establishment of the threshold of ignition based on the criticality of hotspots. The criticality of hotspots in the present study is determined by an ignition criterion given in Barua *et al.*[10] Details are discussed in Sec. II D.

This paper includes four parts. The first part briefly introduces the defective materials studied and the computational framework utilized. Defective PBX 9404 is selected for simulation because the ignition thresholds for perfectly-bonded PBX 9404 have been thoroughly studied in Ref. 1 and agree well with the experimentally measured results.[16–18] The second part predicts the ignition thresholds for the material containing two types of initial defects and the influence of the initial defects on energy dissipation and consequent hotspot distribution in the material microstructures. The third part emphasizes the probabilistic ignition thresholds associated with inherent material heterogeneities. The last part discusses the quantitative relation between the spatial distribution of hotspots and initial defects.

II. FRAMEWORK OF ANALYSIS

A. Materials and microstructures

Energetic granules and a polymer binder are the typical constituents of polymer-bonded explosives (PBXs). HMX (Octahydro-1,3,5,7-tetranitro-1,3,5,7-tetrazocine) has higher energy density than the other commonly used materials for energetic particles and thus becomes an attractive research topic in the past few decades.[19–22] PBX 9404 is HMX based and consists of 94% HMX, 3% Nitrocellulose (NC), and 3% plasticizer in weight fraction.

The microstructures computationally generated in the present study have 81% HMX grain and 19% binder in volume fraction. Although the theoretical volume fraction of HMX in PBX 9404 is 91.5%, Benson and Conley[23] and Mas *et al.*[24] observed that actual fractions in microstructures are lower, owing to the fact that some HMX granules are too small to be resolved and some others are absorbed in the binder. Kim *et al.*[1] employed a set of microstructures of PBX 9404 with a grain volume fraction of 81% to predict the shock ignition thresholds which agree well with experimentally measured thresholds. The present paper uses the same HMX content for PBX microstructures as in Kim *et al.*[1]

Similar to the method used in Kim *et al.*,[1] the polygonal shapes of the HMX granules that are in accordance with the microscopic observation are created by Voronoi tessellation. The average equivalent diameter of the grains is 210 μm and it has a monomodal size distribution whose standard deviation is 66 μm. Details of the microstructural attributes of the two-phase (HMX/binder) PBX and the method used to generate the microstructure are described in Ref. 13. This approach provides us a feasible way to create large numbers of samples with the prescribed statistical attributes and makes it possible to control the overall statistical attributes when generating multiple microstructures.

In addition to variations in constituent morphologies as embodied by the multiple samples, randomly distributed initial defects are also considered in each of the microstructures. Although different types of defects exist simultaneously (cracks inside energetic granules, cracks along granule-binder interfaces or interfacial debonding sites, and voids) and may have a variety of morphologies in real samples (as seen in Fig. 1), it is desirable to delineate and quantify the effects for each type. Here, we focus on the cracks. The reason is twofold: (1) there have been significant studies on the effects of a single void or a small number of voids on the response and reaction of energetic materials using Eulerian computational methods,[22,25–28] and, in contrast, there has been very little study on the effects of cracks, especially the effects of populations of cracks at the microstructure level; and (2) the Lagrangian cohesive finite element framework (CFEM) used here to explicitly resolve and track distributed cracks is less suitable for voids compared with Eulerian frameworks. For these reasons and to separately delineate the effects of each type of cracks, two sets of microstructure samples are used. The first set of microstructures involves defects in the form of pre-existing debonding sites at grain-binder boundaries. These sites of debonded interfaces (interchangeably referred to as interfacial cracks) have surface pairs in contact without cohesion. They can be considered as sites of totally damaged segments of interfaces with varying lengths. Three levels of total damage or overall extent of initial debonding (0%, 50%, and 100%, as shown in Fig. 2) are considered. These levels represent the ratio between the cumulative length of initially debonded grain-binder interfacial sites around each HMX grain and the total grain-binder interface length of that grain. The percentage levels also represent the overall fractions of a sample's debonded interfaces. In the implementation here, each grain has at most one debonding site and its location is randomly assigned. The second set of microstructures involves defects in the form of initial transgranular cracks. Randomly selected grains contain randomly oriented and randomly located

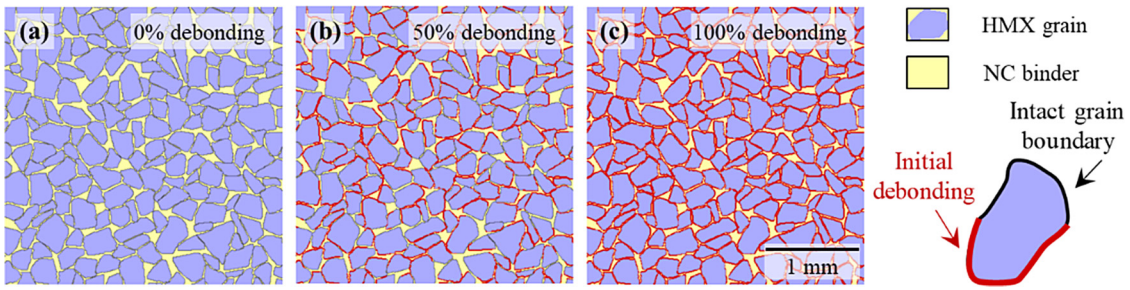

FIG. 2. Microstructures with different levels of initial debonding at grain boundaries: (a) 0%, (b) 50%, and (c) 100%.

through cracks. Each initial crack starts from a random point on a grain boundary, goes straight through a grain, and ends at another point on the boundary. No crack ends in the interior of a grain. Three levels of initial cracking (0%, 10%, and 20%, as shown in Fig. 3) are considered. These levels represent the ratio between the cumulative length of transgranular cracks and the total length of all grain boundaries in a microstructure. In the implementation here, each grain has at most one transgranular crack. The levels of defects chosen here lie in the range of the defect content observed in experiments.[3,29–31] Both initial debonding (interfacial cracks) and initial cracking (transgranular cracks) involve the contacting surface pairs having zero bonding strength, with the rest of the microstructures not involved in the defects having normal bonding.

B. Configuration for analysis

In the experiments of Weingart *et al.*,[16] Gittings,[17] and Trott and Jung,[18] the impact produced by a launched thin flyer generates a loading pulse. The propagation of the loading pulse throughout the specimen is shown in Fig. 2 of Ref. 32. To emulate the experimental conditions, for a specified time duration, a prescribed particle velocity is applied at the impact surface [left boundary of the sample in Fig. 4(a)]. The top, bottom, and right boundaries are constrained to ensure that there is no perpendicular displacement or lateral expansion at the boundaries. This is a two-dimensional plane strain configuration and it is approximately equivalent to the conditions of macroscopic uniaxial strain. The piston velocity (U_p) required can be determined by the impedances (ρU_s) of the flyer and the sample. In the experiments, the loading conditions studied are equivalent to the range of particle velocity $U_p = 371 - 1960\,\mathrm{m/s}$. In the present studies, $U_p = 400 - 1000\,\mathrm{m/s}$. The pulse duration in the present calculations has a range of $\tau = 40$–800 ns, which can be determined by the thickness of the flyer. At each load intensity, successively longer loading pulses are imposed for each sample. Using such a method, the precise condition for ignition at each load intensity can be determined. Table I lists the imposed particle velocity, the range of input energy, the range of pulse durations, and the finest pulse increment that are used in this study. Figure 4(b) shows the time history of the load profile. To eliminate infinite acceleration at the impact surface (left boundary) in Fig. 4(a), in a ramp time of $t_{ramp} = 10$ ns, particle velocity increases from 0 to U_p and is kept constant until $t = \tau$. When $t \geq \tau$, the pulse loading comes to an end and the impact surface (left boundary) is released from the velocity loading.

C. Material behavior

A Lagrangian cohesive finite element method (CFEM)[10–12] is used. This framework ensures that hotspot evolution resulting from thermo-mechanical energy dissipation in the constituents of PBXs under shock pulse loading can be explicitly captured. The grain material follows an elasto-viscoplastic constitutive law that incorporates hydrostatic stress-dependence. The binder follows an elasto-viscoelastic constitutive law. Specifically, to account for the hydrostatic stress-dependence of the material behavior, the hydrostatic part of the stress tensor carried by all the constituents follows the Birch-Murnaghan equation of state or the B-M EOS; the deviatoric part of the stress tensor of the grain material follows the elasto-viscoplastic constitutive law developed by Zhou *et al.*;[33] for the binder, the deviatoric part of the stress follows the Prony series that is defined in Mas *et al.*[34] Cohesive elements are embedded inside each

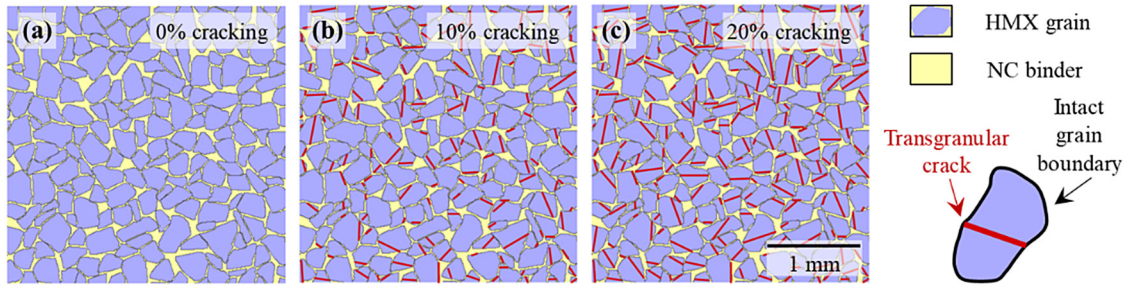

FIG. 3. Microstructures with different levels of initial transgranular cracks in the energetic granules, with total crack length being (a) 0%, (b) 10%, and (c) 20% of total grain boundary length.

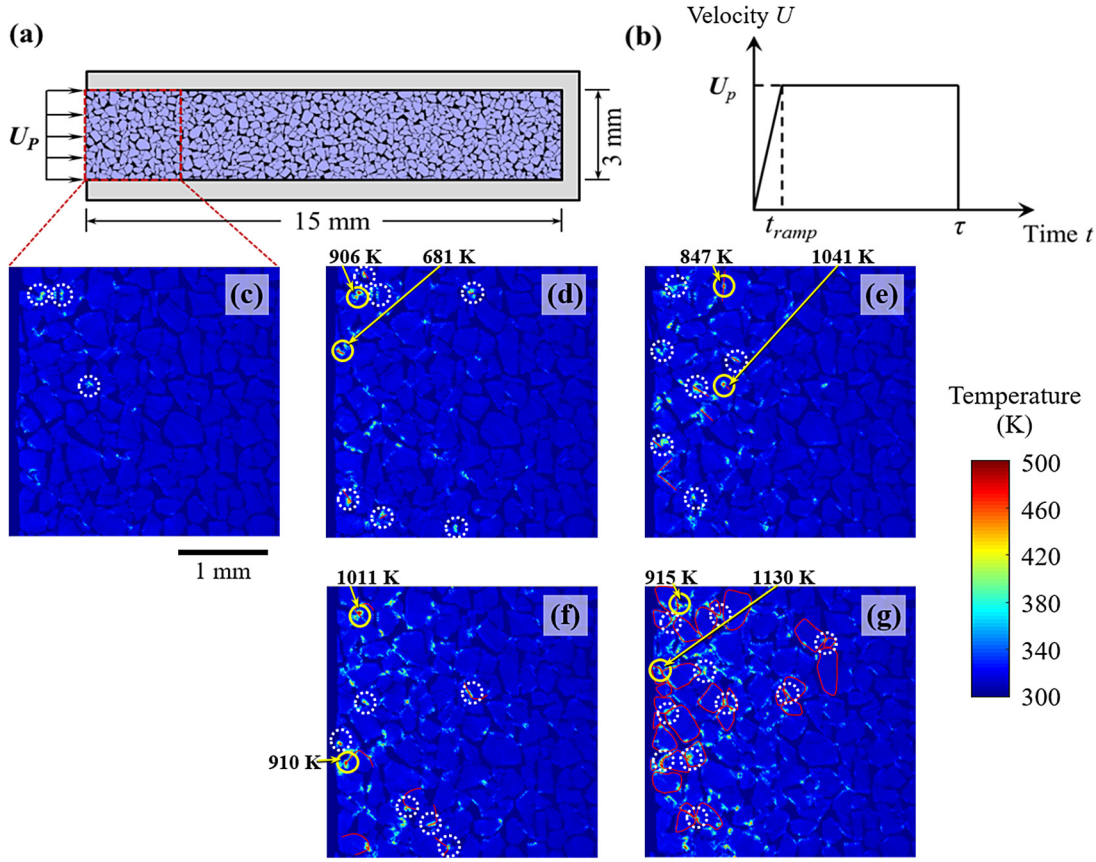

FIG. 4. (a) Loading and boundary conditions of the computational model, (b) history of the velocity applied on the impact face (left boundary), and [(c)–(g)] critical hotspot locations at $t = 1.6\,\mu$s, $U_p = 600$ m/s, and $\tau = 200$ ns in a microstructure; in particular, (c) without initial defects, [(d)–(e)] the same microstructure with initial transgranular cracks [total crack length is 10% (d) or 20% (e) of total grain boundary length], and [(f)–(g)] the same microstructure with 50% (f) or 100% (g) initially debonded grain boundaries. Yellow circles indicate critical hotspots, and white dotted circles indicate some sub-critical hotspots. Red line segments indicate locations of some relevant initial defects. The images provide visual confirmation of the relationship between defects and hotspots.

constituent and at all boundaries between the constituents to account for crack propagation. The bilinear traction-separation law these cohesive elements follow is described in detail by Zhai *et al.*[35] In the present study, initial grain cracking and interfacial debonding are created by assigning zero bonding strength to the corresponding cohesive elements, with the rest having normal bonding. An algorithm given by Hardin[36] is used for contact detection of surfaces after fracture. The surface elements that are in contact are controlled by the Coulomb friction damping model. The mechanical deformation and failure models and Fourier's heat conduction model are coupled to account for material's thermal conduction. Frictional dissipation along interfaces, plastic dissipation, viscoelastic dissipation, and heat conduction are the sources that contribute to the local temperature rise and consequent hotspot development in the PBX under dynamic loading. Details of the algorithm and models are specified in Ref. 12. Parameters of the models and relevant material properties are tabulated in Tables 2–5 by Kim *et al.*[1]

TABLE I. Loading conditions and minimum increments between successive durations.

U_p (m/s)	$P{\cdot}U_p$ (GW/cm^2)	Range of pulse duration t_{pulse} (ns)	Range of E (kJ/cm^2)	Minimum t_{pulse} interval (ns)
400	0.0972	200–1200	0.0185–0.123	40
600	0.243	50–300	0.00892–0.0731	10
800	0.465	30–180	0.00761–0.0819	5
1000	0.773	30–80	0.0121–0.0482	2

D. Criterion for determining the onset of ignition

The initiation of chemical reaction in the energetic phase (grains) is determined by a criterion developed in Refs. 1 and 10 providing a dependence of critical hotspots on their size and temperature,

$$d(T) \geq d_c(T), \tag{1}$$

where d denotes the equivalent hotspot size at or above the temperature of interest (T) developed during a pulse loading. d_c represents the threshold size of a hotspot required to initiate thermal runaway under the given temperature of interest (T). Criticality of HMX on the right-hand side of Eq. (1) is analyzed by Tarver *et al.*[37] using chemical kinetics by considering multistep reaction mechanisms. Their model is advantageous such that both reactants and products are pressure and temperature dependent. The model is thus used to determine the quantitative relation between critical size and temperature of a hotspot in our framework. The left-hand side of Eq. (1) accounts for the calculated temperature fields

in the microstructures. Because there exist temperature variations within each hotspot, a ±10% band relative to the mean is used in the threshold condition, suggesting a hotspot being critical when it is above 90% of the average value. Details of the thresholds can be found in Refs. 1 and 10. Critical and some sub-critical hotspots in a microstructure with different contents of the defect are shown in Figs. 4(c)–4(g).

III. FINDINGS

To account for microstructure randomness, a set of five statistically consistent microstructures with different levels of defects are created as described in Sec. II A. At the impact face, these samples are subject to velocity loading conditions introduced in Sec. II B. Second, the size-temperature initiation criterion delineated in Sec. II D is used to determine whether a hotspot has reached criticality. If the number of critical hotspot reaches a prescribed number in a sample, the sample has reached criticality. Third, the loading conditions under which 50% of the samples achieve ignition are determined. These loading conditions resulting in a 50% ignition probability serve as the basis to obtain the initiation probability throughout the entire loading range using a modified James type relation.[38,39] The results are used to analyze the effects of interfacial and transgranular defects on the ignition thresholds. A microstructure analysis is also carried out to quantify the relationship between hotspot development and defects. To this end, the spatial preference in hotspot distribution is studied and the proximity of hotspots to pre-existing microstructure defects is calculated. It is found that there is a gravitation of hotspots toward initial defects.

A. Ignition threshold

Ignition thresholds for 50% initiation probability are studied and analyzed using the relation proposed by James[38] and modified by Welle *et al.*[39] The relation has a form of

$$\frac{\Pi_c}{\Pi} + \frac{E_c}{E} = 1, \tag{2}$$

where the energy fluence $E = PU_p\tau$ is the amount of energy that has been imparted to the specimen per unit area up to a given time, and the power flux $\Pi = PU_p$ is a measure for the time rate at which work imparted to the material per unit area of the impact face. Π_c and E_c denote the critical power flux and the critical input energy, respectively. By definition, the input energy E is equivalent to time integration of the power flux Π over the pulse duration τ. Equation (2) originates from a shock initiation threshold based on the critical input energy concept introduced by Walker and Wasley.[40] This relation involves an asymptote $\Pi = \Pi_c$ so it can better represent experimental data at low impact velocities. The Appendix in Kim *et al.*[14] contains the detailed derivation. The underlying physical mechanism tracked by Eq. (2) is the fact that as loading rate increases, the amount of energy required to cause ignition decreases. In Figs. 5(a) and 5(b), the computationally obtained thresholds for PBX 9404 with different levels of initial grain boundary debonding [Fig. 5(a)] and initial transgranular cracking [Fig. 5(b)] are compared in the James ($E-\Pi$) space. Each data point in Figs. 5(a) and 5(b) denotes a threshold of 50% ignition probability determined using five microstructures for each loading condition and each defect level. Each dotted curve represents fits of the numerically obtained data to the modified James equation in the form of Eq. (2) for each level of defect. The results in Figs. 5(a) and 5(b) show that increasing load intensity lowers the ignition thresholds in general, as expected. It can also be seen that defects lower the ignition thresholds, with higher levels of defects corresponding to lower ignition thresholds. This trend is consistent with the experiments of Baillou *et al.*[4] and Van der Steen *et al.*[5] on RDX-based PBX. Figures 5(a) and 5(b) also compare the calculated ignition thresholds and available experimental data from Weingart *et al.*,[16] Gittings,[17] and Trott and Jung.[18] Unfortunately, the cited references do not discuss the type and level of defects, or the possible lack of them, in the samples. Since the three separate studies involved samples from at least three

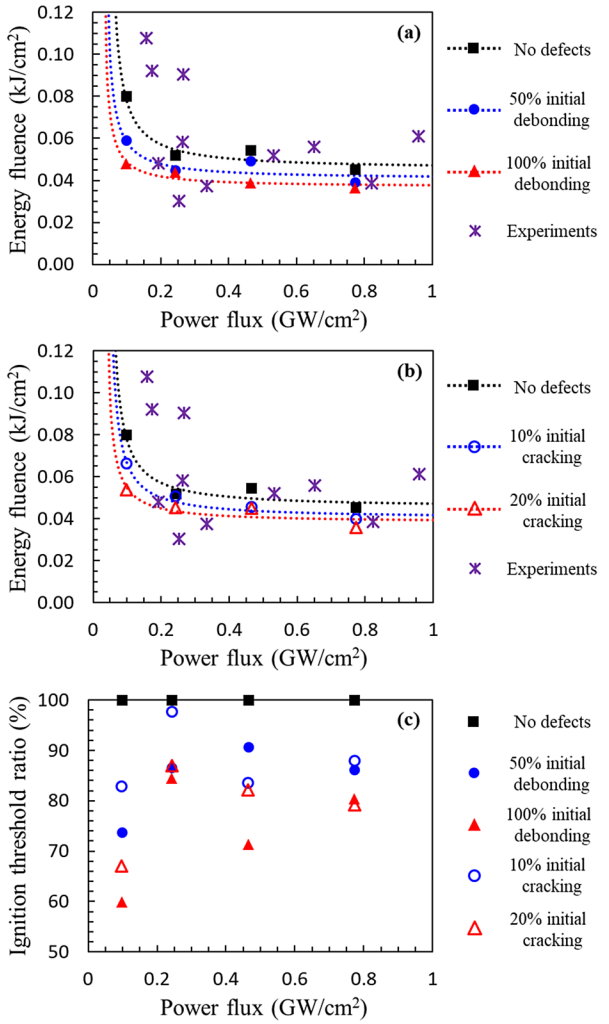

FIG. 5. [(a)–(b)] Thresholds for 50% ignition probability in the E-Π space for PBX 9404 with (a) different levels of initial grain boundary debonding and (b) different levels of initial transgranular cracking. The dotted lines represent fits to the James relation ($\Pi_c/\Pi + E_c/E = 1$). Experimental data "✱" are from Weingart *et al.*,[16] Gittings,[17] and Trott and Jung.[18] (c) The ratio between 50% ignition thresholds (in terms of energy fluence) of PBX 9404 with and without initial defects, with the ignition threshold of the intact material [black data points in (a)–(b)] being 100% for each load intensity.

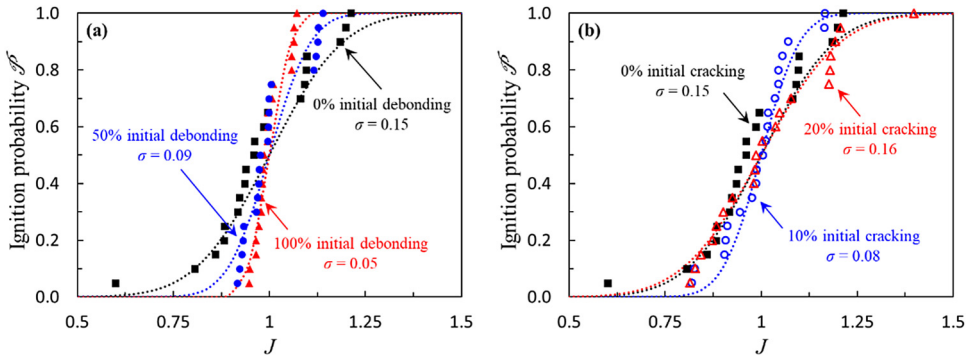

FIG. 6. Ignition probabilities as a function of the James number J for PBX 9404 with (a) initial grain boundary debonding and (b) initial transgranular cracking. $J = 1$ corresponds to a probability of 50%.

independent sources and batches, there is a significant amount of scatter in the experimental data, due to sample variations in terms of microstructure, defects, and preparation. However, the calculated results are in general agreement with the experimental results. Since micrographs are not available for the materials used in the experiments, it is not possible to, at this time, ascertain and delineate the effect of defects in the experimental data. As such, it is desirable to have experimental results that systematically address the effects of defects. Part of this will have to involve systematic control of defects in the manufacturing process. In Fig. 5(c), quantitative comparisons between the 50% ignition thresholds (in terms of energy fluence) for PBX 9404 with and without defects are graphed, with the threshold of the intact material being 100% for each load intensity. It quantitatively provides information regarding the influence of the initial defects on the 50% probability threshold. Consistent with the experimental observation of Borne,[6,7] the effect of initial defects decreases as loading rate increases, as indicated by the converging threshold curves in Figs. 5(a) and 5(b) and the converging data points representing different defect levels in Fig. 5(c) in the high load intensity region. These observations are applicable to both types of defects.

B. Ignition probability map

The data points and curves in Fig. 5 show the thresholds for a 50% ignition probability. These 50% probability thresholds are determined using multiple microstructure samples subjected to the same loading conditions. Just like multiple samples in experiments allow the statistical distribution of a material property (ignition threshold in this case) to be quantified, the multiple statistically similar samples (microstructures) in the calculations allow the ignition threshold corresponding to any ignition probability level to be determined. Conversely, the use of multiple statistically similar samples (microstructures) also offers a mechanism to determine the probability of ignition for any macroscopic loading condition as represented by any point (E,Π) in the James space shown in Figs. 5(a) and 5(b). As pointed out by Gresshoff and Hrousis,[41] probable causes of the statistical variation of measured ignition behavior include uncertainties from experimental conditions and effects of material heterogeneities inherent in the samples. Although both types of stochasticity exist in experiments, only the latter is considered in the present study. Gresshoff and Hrousis[41] further modified the James criterion and introduced the James number J, a quantitative measure that facilitates probabilistic analysis. The modified James relation is in the form of

$$\frac{\Pi_c}{\Pi} + \frac{E_c}{E} = \frac{1}{J}. \tag{3}$$

When $J = 1$, Eq. (3) is equivalent to the James relation with a 50% initiation probability in Eq. (2); when $J > 1$, it corresponds to the loading conditions under which more than 50% of the samples reach criticality; and when $J < 1$, conditions that result in lower than 50% ignition probabilities are implied.

Figure 6(a) shows the computationally determined ignition probabilities for PBX 9404 with initially debonded grain boundaries, and Fig. 6(b) shows the corresponding results for PBX 9404 with initial transgranular cracks as a function of the James number J. Note that $J = 1$ corresponds to a probability of 50% by definition. The data points are analyzed using the Gaussian distribution function as

$$\begin{aligned}\mathscr{P}(J) &= \frac{1}{\sigma\sqrt{2\pi}} \int_{-\infty}^{J} \exp\left[-\frac{(x-1)^2}{2\sigma^2}\right] dx \\ &= \frac{1}{2}\left[1 + \operatorname{erf}\left(\frac{J-1}{\sqrt{2}\sigma}\right)\right]\end{aligned} \tag{4}$$

TABLE II. Parameters in James initiation thresholds and standard deviations presented in Fig. 6.

Condition of PBX 9404	Π_c (GW/cm^2)	E_c (kJ/cm^2)	σ
No defects	0.0420	0.0451	0.15
50% initial debonding	0.0303	0.0407	0.085
100% initial debonding	0.0242	0.0369	0.045
10% initial cracking	0.0398	0.0402	0.079
20% initial cracking	0.0299	0.0381	0.16

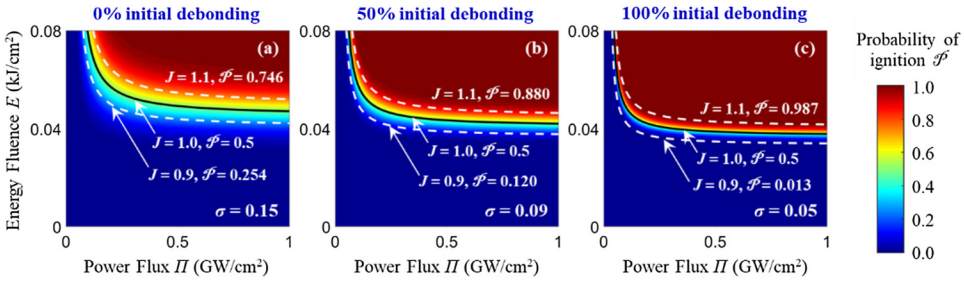

FIG. 7. Ignition probability maps for PBX 9404 with initial grain boundary debonding levels of (a) 0%, (b) 50%, and (c) 100%.

and

$$\mathscr{P}(E, \Pi) = \frac{1}{2} + \frac{1}{2}\mathrm{erf}\left[\frac{1}{\sqrt{2}\sigma}\left(\frac{E\Pi}{\Pi E_c + E\Pi_c} - 1\right)\right]. \quad (5)$$

In Eqs. (4) and (5), σ is the standard deviation. Similar to E_c and Π_c, it is another material constant that can be determined by fitting to the data points obtained either from experiments or from the computations carried out here. The values of σ, E_c, and Π_c acquired from the present analysis are given in Table II. The ignition probability $\mathscr{P}$ corresponding to E and Π can be obtained using Eq. (5). Conversely, Eqs. (3)–(5) also allow the thresholds (or loading envelop) for any level of ignition probability between 0 and 1 to be calculated. Consequently, the material-dependent ignition probability maps are created based on Eq. (5) in the James ($E-\Pi$) space for PBX 9404 with different levels of initial debonding shown in Fig. 7 and different levels of initial cracking in Fig. 8. As is shown in Figs. 7 and 8, the ignition probability is a strong function of defect level and distribution. Again, materials with a higher defect level have higher probabilities to ignite under the same load intensities.

C. Energy dissipation and hotspot distribution

To delineate the primary factors affecting the differences in the behavior of the materials with different levels of defects, the dissipation under two impact velocities $U_p = 600$ and 1000 m/s are analyzed. To this end, the distributions of total energy dissipation and frictional dissipation along the specimen length away from the impact surface are analyzed. The results for cases with different levels of initial debonding are shown in Fig. 9, and the results for cases with different levels of initial grain cracking are shown in Fig. 10. Clearly, frictional dissipation alone accounts for essentially all the differences in total energy dissipation among the cases with different defect levels, although other dissipation mechanisms contribute significantly to the total dissipation. Previous experimental[42] and theoretical[43] studies have shown that internal friction of closed cracks is one of the most important heating mechanisms. Consequently, as interfacial or grain defects are introduced, the additional internal surface pairs serve as sites for internal frictional dissipation and heating. This additional source of heating is the primary driving force behind the changes in ignition behavior associated with the defects. Note in Figs. 9 and 10 that the differences in frictional dissipation (and therefore total dissipation) among the cases with different defect levels decrease as the impact velocity increases, suggesting that, at high load intensities, the perturbations given by defects play a less important role overall and other material heterogeneities inherent in the microstructure dominate. Another factor at work is that, under high-intensity loading, the energy dissipated is more localized near the impact surface and more localized in shear bands and along cracks and interfaces. As a result, hotspot criticality is attained over a shorter time period requiring a lower overall energy input to the materials. This is another factor leading to smaller differences among the different cases.

We use $T_{cut} = 400$ K as the cutoff temperature of a hotspot as in Kim *et al.*,[1] where profiles of hotspot density for PBX 9404 samples under different shock load intensities with $U_p = 200$–1200 m/s are studied. This T_{cut} is set such that meaningful trends of hotspot distribution can be obtained. Hotspots in the microstructures under two load intensities are analyzed in Fig. 11 (interfacial debonding cases) and Fig. 12 (grain crack cases). Overall, hotspot density increases with load intensity and with defect level. For materials with either type of defects, the hotspots are more sparsely distributed throughout the materials at lower load intensities and more concentrated near the loading site (left end) at higher load intensities. Also, the difference in hotspot density between cases with different defect levels is significant under low load intensities but is negligible under high load intensities. These trends in hotspot distribution echo and are in good accordance with the trends in energy dissipation.

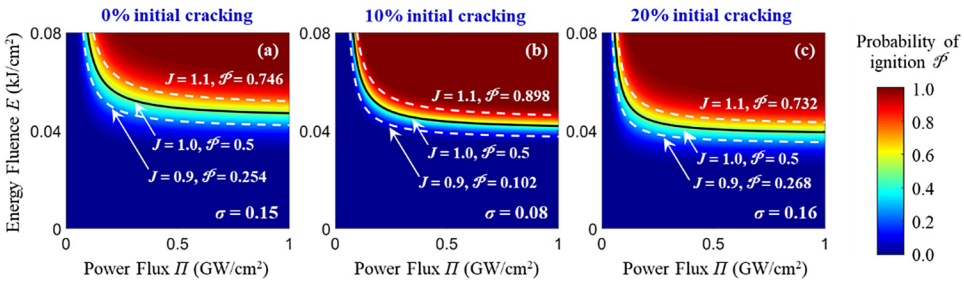

FIG. 8. Ignition probability maps for PBX 9404 with initial transgranular cracking levels of (a) 0%, (b) 10%, and (c) 20%.

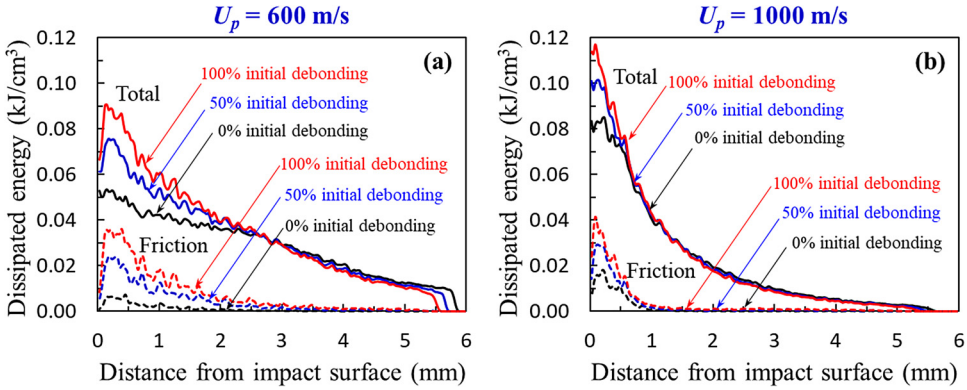

FIG. 9. Profiles of total energy dissipation and dissipation due to friction for PBX 9404 with different levels of initial debonding: (a) $U_p = 600$ m/s, $\tau = 200$ ns, and $t = 1.6\,\mu$s and (b) $U_p = 1000$ m/s, $\tau = 60$ ns, and $t = 1.6\,\mu$s.

D. Relationships between hotspots and initial defects

As is shown in Figs. 4(c)–4(g), most hotspots are located at the grain boundaries. As initial defects are introduced in the microstructure, both critical and sub-critical hotspots gravitate toward the defects. To further understand the mechanisms of hotspot formation, the spatial relationships between hotspot formation and initial defects are quantitatively studied. For the materials with 50% initially debonded grain-binder boundaries, the distances between hotspots and their nearest initially debonded interface segments and the nearest intact interface, as illustrated and defined in Fig. 13, are calculated. The cumulative results are shown in Fig. 13 in histogram form. The error bars in the figure represent variations among the multiple samples in each case, and the bars represent averages of the multiple samples. The height of each bar A_{HS}/A_{HS}^{total} denotes the total area of hotspots that lie within a certain range of distance from the nearest initially intact [Figs. 13(a)–13(c)] or debonded [Figs. 13(d)–13(f)] interface as a fraction of the total hotspot area in the sample. First, regardless of load intensity, most hotspots are located within 30 μm from the nearest grain boundary (defective or intact). Since the average equivalent diameter of the HMX grains is around 210 μm, hotspots tend to form at and are significantly influenced by grain boundaries regardless of defects. With that general trend in mind, we look at the effects of defects on hotspots. When the impact velocity is $U_p = 400$ m/s, nearly all hotspots (>90% of hotspots) form near debonded interfacial sites (defects); in contrast, the hotspots are generally farther from intact interfaces [see the first bars from the left in Figs. 13(a) and 13(d)]. Note that the microstructures here happen to have equal amounts of initially debonded and initially intact grain boundaries; nevertheless, the results apply to microstructures with more or less defective grain boundaries as well. As the impact velocity U_p increases to 600 m/s, the gravitation of hotspots toward grain-binder interfaces and defective interfacial sites (>80% of hotspots closer to defective sites) is still strong [see the first bars from the left in Figs. 13(b) and 13(e)], but not as strong as that seen at $U_p = 400$ m/s. However, when U_p increases to 1000 m/s, a relatively high load intensity, the hotspots are nearly evenly distributed from defective or intact interfaces and the spatial bias toward defects has largely vanished, with only ~30% more hotspots closer to defective sites [see first bars from the left in Figs. 13(c) and 13(f)].

The effect of transgranular cracks is similar. For the material with a transgranular crack level of 20% (total length of such cracks is equal to 20% of the total grain boundary length, a level with roughly each grain containing one transgranular crack), Fig. 14 shows the distribution of the distance of hotspots to their corresponding nearest grain boundary and initial in-grain crack. Note that in this case, the grain boundaries are fully intact and there is no interfacial defect. Again, as is the case for microstructures with grain boundary defects, the hotspots are closer to the grain boundaries. Since the total length of the grain boundaries is much higher than the total length of the in-grain cracks, it is unsurprising to find that hotspots clearly gravitate toward grain boundaries.

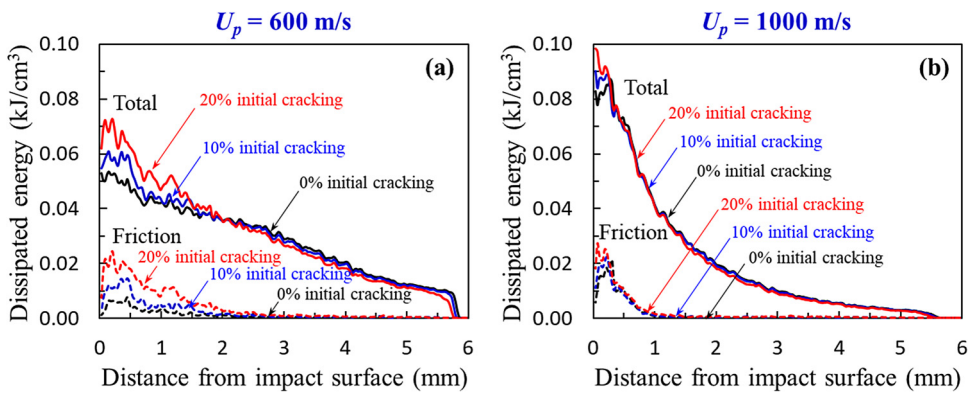

FIG. 10. Profiles of total energy dissipation and dissipation due to friction for PBX 9404 with different levels of initial cracking: (a) $U_p = 600$ m/s, $\tau = 200$ ns, and $t = 1.6\,\mu$s and (b) $U_p = 1000$ m/s, $\tau = 60$ ns, and $t = 1.6\,\mu$s.

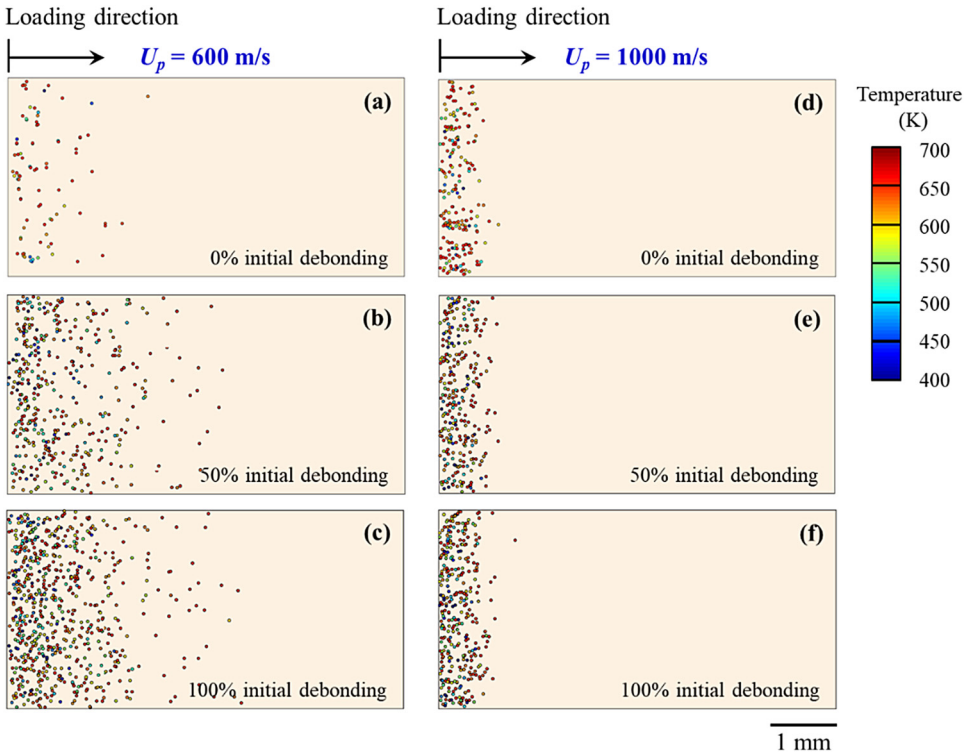

FIG. 11. Hotspot distributions under $U_p = 600$ m/s ($\tau = 200$ ns, and $t = 1.6$ μs) for PBX 9404 with different levels of initial debonding at grain boundaries (a) 0%, (b) 50%, and (c) 100%, and under $U_p = 1000$ m/s ($\tau = 60$ ns and $t = 1.6$ μs) for PBX 9404 with different levels of initial debonding at grain boundaries (d) 0%, (e) 50%, and (f) 100%.

This proximity of hotspots to grain boundaries relative to in-grain cracks illustrates the dominant role of the grain-binder interfaces in the development of hotspots and consequently the ignition of the materials. Nevertheless, it can be seen from Fig. 14 that as the impact intensity increases, fewer hotspots are developed close to the defects (in-grain cracks), as in the case for materials with interfacial defects discussed earlier.

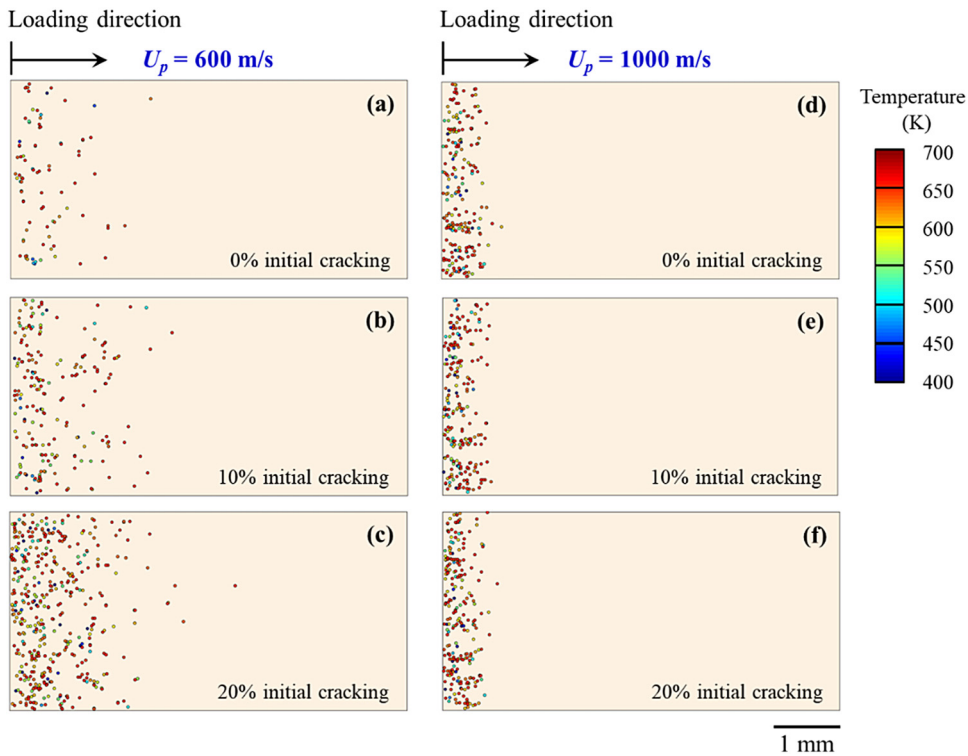

FIG. 12. Hotspot distributions under $U_p = 600$ m/s ($\tau = 200$ ns and $t = 1.6$ μs) for PBX 9404 with different levels of initial transgranular cracks in the energetic granules, with total crack length being (a) 0%, (b) 10%, and (c) 20% of total grain boundary length, and under $U_p = 1000$ m/s ($\tau = 60$ ns and $t = 1.6$ μs) for PBX 9404 with different levels of initial transgranular cracks in the energetic granules, with total crack length being (d) 0%, (e) 10%, and (f) 20% of total grain boundary length.

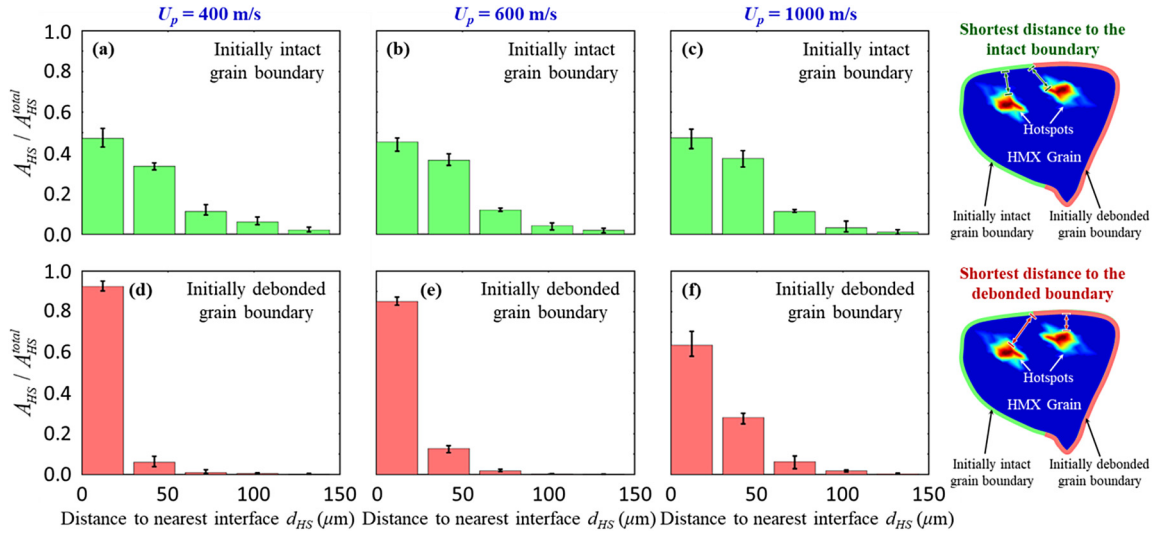

FIG. 13. Proximity of hotspot to initially intact grain boundary at $t = 1.6\,\mu$s under (a) $U_p = 400$ m/s ($\tau = 560$ ns), (b) $U_p = 600$ m/s ($\tau = 200$ ns), and (c) $U_p = 1000$ m/s ($\tau = 60$ ns), and to initially debonded grain boundary at $t = 1.6\,\mu$s under (d) $U_p = 400$ m/s ($\tau = 560$ ns), (e) $U_p = 600$ m/s ($\tau = 200$ ns), and (f) $U_p = 1000$ m/s ($\tau = 60$ ns). Material is PBX 9404 with 50% initially debonded grain-binder boundaries.

To quantify the association with or gravitation toward defects of hotspots, an empirical parameter which we call the "defect preference ratio" or r_{pref} is defined and calculated. For materials with interfacial defects, this parameter has the form of

$$r_{pref} = (A_{HS}^{debonded} - A_{HS}^{intact})/A_{HS}^{total}, \tag{6}$$

where $A_{HS}^{debonded}$ denotes the total area of hotspots within $30\,\mu$m (the first distance range in Fig. 13) of an interfacial defect, A_{HS}^{intact} denotes the total area of hotspots within $30\,\mu$m of an intact interface, and A_{HS}^{total} is the total area of all hotspots in the sample. If hotspots have no spatial bias toward defects, $r_{pref} = 0$; if hotspots gravitate toward defects, $r_{pref} > 0$; and if hotspots have closer proximity to intact interfaces, $r_{pref} < 0$. For materials with intragranular cracks, this parameter has the form of

$$r_{pref} = (A_{HS}^{crack} - A_{HS}^{intact})/A_{HS}^{total}, \tag{7}$$

where A_{HS}^{crack} is the total area of hotspots within $30\,\mu$m (the first distance range in Fig. 14) of a transgranular crack and A_{HS}^{intact} denotes the total area of hotspots within $30\,\mu$m of a grain boundary as all grain-binder interfaces are defect-free (intact).

Graphically, r_{pref} is the difference in the heights of the first (left most) bars in Figs. 13 and 14. For instance, the first bars in Figs. 13(a) and 13(d) give r_{pref} for materials with 50% interfacial defects under a load intensity of 400 m/s. Similarly, the first bars in Figs. 14(a) and 14(d) give r_{pref} for materials with 20% intragranular cracks under a load intensity of 400 m/s. As shown in Fig. 15, r_{pref} decreases steadily

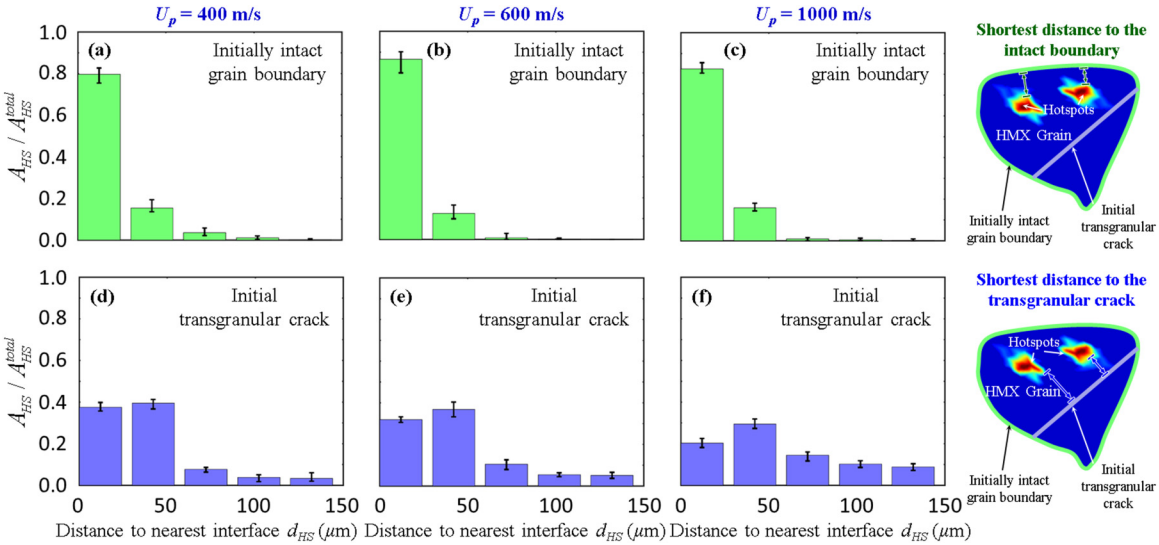

FIG. 14. Proximity of hotspot to grain boundary at $t = 1.6\,\mu$s under (a) $U_p = 400$ m/s ($\tau = 560$ ns), (b) $U_p = 600$ m/s ($\tau = 200$ ns), and (c) $U_p = 1000$ m/s ($\tau = 60$ ns), and to initial grain crack at $t = 1.6\,\mu$s under (d) $U_p = 400$ m/s ($\tau = 560$ ns), (e) $U_p = 600$ m/s ($\tau = 200$ ns), and (f) $U_p = 1000$ m/s ($\tau = 60$ ns). Material is PBX 9404 with initial transgranular cracks whose total length is equal to 20% of the total grain boundary length.

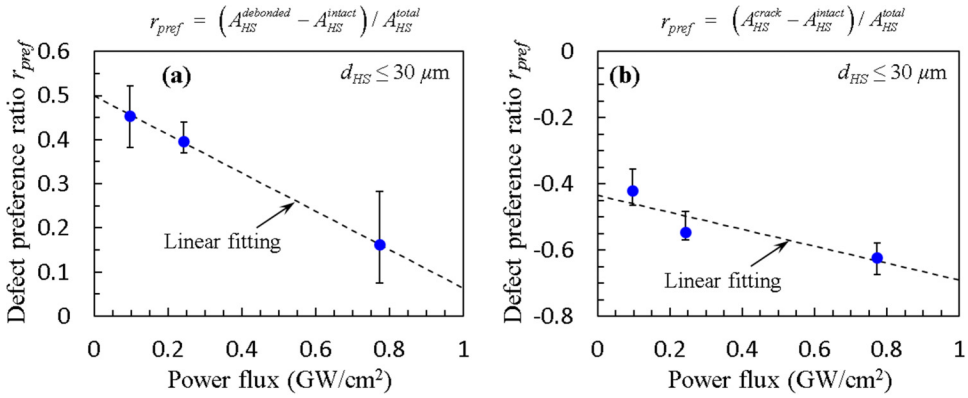

FIG. 15. Defect preference ratio r_{pref} as a function of load intensity for (a) PBX 9404 with 50% initially debonded grain-binder boundaries and (b) PBX 9404 with transgranular cracks whose total length is equal to 20% of the total grain boundary length.

as power flux (a measure for load intensity) increases for materials with both types of defects. This, again, reflects the fact that the association of hotspots with initial defects diminishes as load intensity increases. For materials with interfacial defects [Fig. 15(a)], $r_{pref} > 0$, indicating gravitation of hotspots toward defects. For materials with intragranular cracks [Fig. 15(b)], $r_{pref} < 0$, indicating a stronger association of hotspots with grain boundaries or the influence of grain boundaries on the development of hotspots is stronger than the influence of in-grain cracks. Figure 15 provides a means to estimate by extrapolation the load intensity at which materials with and without defects (interfacial debonding or transgranular cracks) would have the same ignition probability. For the cases with interfacial debonding [Fig. 15(a)], this threshold intensity is approximately 1.2 GW/cm^2 in terms of the power flux and 1200 m/s in terms of the impact velocity.

Under overall compressive loading, cracks are closed and sliding along crack faces is the dominant mode of fracture development and contribution to the overall deformation of the materials. As such, shear stresses along cracks provide the primary driving force for the crack development. For the nominally uniaxial strain state of the impact loading considered, shear stresses on average are maximum along ±45° directions relative to the loading direction. Consequently, cracks that are along these directions tend to show higher amounts of sliding and lead to more extensive frictional and constituent inelasticity heating. How does this manifest under different load intensities? Here, the distribution of hotspots along cracks of different orientations is also analyzed to answer this question. Figure 16 shows the spatial correlation between hotspots and transgranular cracks for the set of samples analyzed in Fig. 14. Only two levels of load intensity ($U_P = 400$ m/s and $U_P = 600$ m/s) are shown and the result reflects the aggregate behavior of five samples in each case. The circumferential coordinate (angle) denotes the angle between the crack and the loading direction. For each direction, the radial coordinate length denotes the fraction of hotspots that lie within 50 μm of a transgranular crack in the same grain. At $U_p = 400$ m/s [Fig. 16(a)], a majority of the hotspots develop along cracks that are about ±45° relative to the loading direction, giving rise to two long "wings" in the plot. This gravitation toward the ±45° directions reflects the effects of the intragranular cracks on the overall behavior. In contrast, very few hotspots are generated adjacent to cracks either parallel or perpendicular to the loading direction. At $U_p = 600$ m/s [Fig. 16(b)], on the other hand, hotspots develop more equally along all directions, indicating relatively a diminished effect of the intragranular cracks on the overall behavior. In other words, other material heterogeneities intrinsic in the microstructures, such as constituent

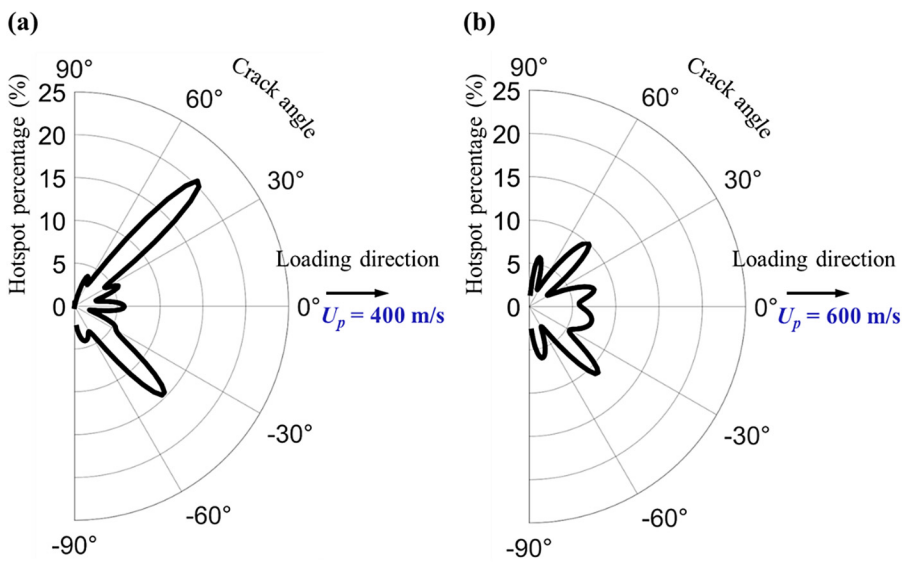

FIG. 16. Distribution of hotspots along cracks of different orientations for materials with initial in-grain cracks at $t = 1.6\ \mu$s: (a) $U_p = 400$ m/s and $\tau = 560$ ns and (b) $U_p = 600$ m/s and $\tau = 200$ ns.

property differences, grain size and shape, grain-binder interfaces, and interfacial bonding strength, play more dominant roles under the higher load intensity. This finding is consistent with the observation made from Figs. 13–15.

IV. CONCLUSIONS

The ignition behavior of PBX 9404, a polymer-bonded explosive, with various configurations of initial defects is analyzed via mesoscale simulations that explicitly account for microstructural heterogeneities, constituent responses of the HMX energetic grains and nitrocellulose binder, and attributes of the interfaces between the constituents. The analysis focuses on the prediction and quantification of the ignition thresholds. The simulations allow mechanical and thermal processes including elasto-viscoplasticity, elasto-viscoelasticity, fracture, crack propagation, frictional heating along the cracks, and heat conduction to be effectively tracked. The trends of the predicted initiation thresholds with different levels of defects are in good agreement with experimental results reported in the literature.[4–8]

The initiation thresholds are analyzed and quantified using the modified James relation ($\Pi_c/\Pi + E_c/E = 1$). Probability distribution function that explicitly quantifies the stochastic initiation behavior is expressed as a function of loading parameters in the James (E-Π) space. Although only the James space is used here, similar analyses can be carried out in other load spaces.

The ignition thresholds of PBX 9404 with different levels of initial defects are compared and the differences are explained through analyses of energy dissipation and consequent hotspot distribution. The spatial distribution of hotspots in relation to defects in the forms of inter-constituent interfacial debonding and transgranular cracks in the energetic grains is studied and quantified using the defect preference ratio r_{pref}. The analysis reveals that defects have a significant effect on the development of hotspots and consequently a strong influence on the ignition thresholds, with the predominant trend being that defects induce hotspots and lower ignition thresholds. The effect and influence are pronounced at lower load intensities and diminish at higher load intensities ($U_p \geq 600$ m/s). This finding points out that, at high load intensities, constituent behavior and the microstructural morphological heterogeneities intrinsic in the material dominate and defects only play a secondary role in determining the ignition behavior of the energetic material.

Although one material system with two constituents is analyzed, the analyses here can be carried out for other material systems with different combinations of constituents, including systems with only one constituent (e.g., pressed energetic granules) and composite systems with multiple constituents (e.g., energetic granules, metallic fuel particles, a binder, and an oxidizer).

It should be noted that the present paper has only examined the effect of initial debonding at grain boundaries and the effect of initial transgranular straight cracks in grains separately. The interactions between the two types of defects when they are present simultaneously have not been considered. How different types of defects interact with each other and whether their combined effect on ignition behavior is a simple superposition or more complex manifestation are topics for future studies. In addition, other types of defects such as micropores[22,25–28,44] and grain cracks with other in-grain morphologies[3] have not been considered here. The framework used here lends itself to the analyses of such defects.

Finally, as we noted in Sec. III A that, at present, there is only a very limited amount of experimental data on the ignition thresholds of the PBX studied here (and, for that matter, other energetic materials as well). Further experimental studies will provide further impetus to analysis on this topic.

ACKNOWLEDGMENTS

Funding from the Air Force Office of Scientific Research (Dr. Martin Schmidt) under Grant No. FA9550-15-1-0499 and the Defense Threat Reduction Agency (DTRA) (Dr. Douglas Allen Dalton) under Grant No. HDTRA1-18-1-0004 is gratefully acknowledged. Part of the calculations were performed using supercomputers at the ERDC and AFRL DSRCs of the U.S. DoD High Performance Computing Modernization Program.

[1]S. Kim, Y. Wei, Y. Horie, and M. Zhou, J. Mech. Phys. Solids **114**, 97 (2018).
[2]S. M. Walley, J. E. Field, and M. W. Greenaway, Mater. Sci. Technol. **22**, 402 (2006).
[3]C. Skidmore, D. Phillips, P. Howe, J. Mang, and J. Romero, in 11th International Symposium on Detonation, Snowmass Village, CO, 1998.
[4]F. Baillou, J. Dartyge, C. Spyckerelle, and J. Mala, in 10th International Symposium on Detonation, Boston, MA, 1993.
[5]A. Van der Steen, H. Verbeek, and J. Meulenbrugge, in *9th International Symposium on Detonation* (Office of Naval Research, 1989), p. 86.
[6]L. Borne, in *10th International Symposium on Detonation* (Office of Naval Research, 1993), p. 286.
[7]L. Borne, in *11th International Symposium on Detonation* (Office of Naval Research, 1998), p. 33300.
[8]R. M. Doherty and D. S. Watt, Propell. Explos. Pyrot. **33**, 4 (2008).
[9]U. Teipel, *Energetic Materials: Particle Processing and Characterization* (John Wiley & Sons, 2006).
[10]A. Barua, S. Kim, Y. Horie, and M. Zhou, J. Appl. Phys. **113**, 064906 (2013).
[11]A. Barua, S. Kim, Y. Horie, and M. Zhou, J. Appl. Phys. **113**, 184907 (2013).
[12]A. Barua and M. Zhou, Model. Simul. Mater. Sci. Eng. **19**, 055001 (2011).
[13]S. Kim, A. Barua, Y. Horie, and M. Zhou, J. Appl. Phys. **115**, 174902 (2014).
[14]S. Kim, C. Miller, Y. Horie, C. Molek, E. Welle, and M. Zhou, J. Appl. Phys. **120**, 115902 (2016).
[15]H. R. James and B. D. Lambourn, J. Appl. Phys. **100**, 084906 (2006).
[16]R. C. Weingart, R. K. Jackson, C. A. Honodel, and R. S. Lee, Propell. Explos. **5**, 158 (1980).
[17]E. F. Gittings, in *Proceedings of the Fourth International Symposium on Detonation, Office of Naval Research, Arlington, TX* (Office of Naval Research, 1965), p. 373.
[18]B. D. Trott and R. G. Jung, in *Proceedings of the Fifth International Symposium on Detonation Pasadena, CA* (Office of Naval Research, 1970), p. 191.
[19]D. E. Christiansen and J. W. Taylor, *HE Sensitivity Study*, Report No. LA-5440-MS, 1973.
[20]D. B. Hayes, in *6th International Detonation Symposium, Coronado, CA* (Office of Naval Research, 1976), p. 95.
[21]J. G. Bennett, K. S. Haberman, J. N. Johnson, and B. W. Asay, J. Mech. Phys. Solids **46**, 2303 (1998).
[22]R. A. Austin, N. R. Barton, J. E. Reaugh, and L. E. Fried, J. Appl. Phys. **117**, 185902 (2015).

[23]D. J. Benson and P. Conley, Model. Simul. Mater. Sci. Eng. **7**, 333 (1999).
[24]E. M. Mas, B. E. Clements, A. Ionita, and P. Peterson, AIP Conf. Proc. **845**, 487 (2006).
[25]L. Tran and H. S. Udaykumar, J. Propul. Power **22**, 959 (2006).
[26]N. R. Barton, N. W. Winter, and J. E. Reaugh, Model. Simul. Mater. Sci. Eng. **17**, 035003 (2009).
[27]A. Kapahi and H. S. Udaykumar, Shock Waves **25**, 177 (2015).
[28]N. K. Rai and H. S. Udaykumar, Phys. Rev. Fluids **3**, 033201 (2018).
[29]P. D. Peterson, J. T. Mang, and B. W. Asay, J. Appl. Phys. **97**, 093507 (2005).
[30]R. K. Govier, G. T. Gray, and W. R. Blumenthal, Metall. Mater. Trans. A **39**, 535 (2008).
[31]H. Guo, J. R. Luo, P. A. Shi, and J. G. Xu, Defense Technology **10**, 154 (2014).
[32]H. K. Springer, C. M. Tarver, J. E. Reaugh, and C. M. May, J. Phys.: Conf. Ser. **500**, 052041 (2014).
[33]M. Zhou, A. Needleman, and R. J. Clifton, J. Mech. Phys. Solids **42**, 423 (1994).
[34]E. M. Mas, B. E. Clements, B. Blumenthal, C. M. Cady, G. T. Gray, and C. Liu, AIP Conf. Proc. **620**, 661 (2002).
[35]J. Zhai, V. Tomar, and M. Zhou, J. Eng. Mater. Technol.-Trans. ASME **126**, 179 (2004).
[36]D. B. Hardin, Thesis, Georgia Institute of Technology, 2015.
[37]C. M. Tarver, S. K. Chidester, and A. L. Nichols, J. Phys. Chem. **100**, 5794 (1996).
[38]H. R. James, Propell. Explos. Pyrot. **21**, 8 (1996).
[39]E. J. Welle, C. D. Molek, R. R. Wixom, and P. Samuels, J. Phys.: Conf. Ser. **500**, 052049 (2014).
[40]F. E. Walker and R. J. Wasley, Explosivstoffe **17**, 9 (1969).
[41]M. Gresshoff and C. A. Hrousis, in 14th International Detonation Symposium, Coeur d'Alene, ID, 2010.
[42]J. E. Field, N. K. Bourne, S. J. P. Palmer, S. M. Walley, and J. M. Smallwood, Philos. Trans. R. Soc. London Ser. A **339**, 269 (1992).
[43]J. K. Dienes, MRS Proc. **24**, 373 (1983).
[44]C. D. Yarrington, R. R. Wixom, and D. L. Damm, J. Appl. Phys. **123**, 105901 (2018).